Analysis of Incident Field Modeling and Incident/Scattered Field Calibration Techniques in Microwave Tomography

Majid Ostadrahimi, *Student Member, IEEE*, Puyan Mojabi, *Member, IEEE*, Colin Gilmore, *Member, IEEE*, Amer Zakaria, *Student Member, IEEE*, Sima Noghanian, *Senior Member, IEEE*, Stephen Pistorius, *Senior Member, IEEE*, and Joe LoVetri, *Senior Member, IEEE*

***Abstract*—Imaging with microwave tomography systems requires both the incident field within the imaging domain as well as calibration factors that convert the collected data to corresponding data in the numerical model used for inversion. The numerical model makes various simplifying assumptions, e.g., 2-D versus 3-D wave propagation, which the calibration coefficients are meant to take into account. For an air-based microwave tomography system, we study two types of calibration techniques—incident and scattered field calibration—combined with two different incident field models: a 2-D line-source and an incident field from full-wave 3-D simulation of the tomography system. Although the 2-D line-source approximation does not accurately model incident field in our system, the use of scattered field calibration with the 2-D line-source provides similar or better images to incident and scattered field calibration with an accurate incident field. Thus, if scattered field calibration is used, a simple (but inaccurate) incident field is acceptable for our microwave tomography system. While not strictly generalizable, we expect our methodology to be applicable to most other microwave tomography systems.**

***Index Terms*—Calibration, imaging, microwave tomography (MWT), modeling.**

I. Introduction

In microwave tomography (MWT), a quantitative map, or *image*, of the dielectric properties of an object of interest (OI) is obtained from a limited set of electromagnetic field measurements made outside the OI. An inverse scattering algorithm is then utilized to reconstruct the image from the measurement data [1]. Inversion algorithms: 1) require the input of an incident field inside the imaging domain; and 2) require calibration of experimental data. This is because the algorithms assume an idealized electromagnetic model of the physical system that simplifies, or ignores, the antennas (field-probes), the finite extent of the imaging chamber, as well as cables leading from the transmitter/receiver instrumentation to the antennas and often makes a 2-D assumption about 3-D wave propagation. The process of calibration may be viewed as an attempt to convert collected experimental data to the assumed numerical model. In addition, though only circuit quantities can be directly measured, most inversion algorithms require field values at appropriate spatial locations/regions within their assumed electromagnetic model. For example, both the Gauss–Newton Inversion (GNI) [2] and the Contrast Source Inversion (CSI) techniques [3] require scattered field quantities at several measurement points surrounding the OI as well as an accurate characterization of the incident field inside the imaging domain.

To reduce the errors associated with the calibration, it is beneficial to constrain the design of MWT systems, e.g., use antennas that can be modeled simply and use a lossy matching fluid so that the mutual coupling between co-resident antennas as well as the effect of the chamber boundaries and feed cables can be minimized. Even when such design considerations are taken into account, the calibration process will not be perfect, and the incident field used in the algorithms will still only approximate the true incident field. The resulting error, due to these two factors, contributes to what is called modeling error.

In this letter, we consider: 1) two different incident field models inside the imaging domain, and 2) two different calibration techniques for a 2-D air-based MWT system. Incident fields are either modeled as a simple 2-D line-source or as a single plane of a full vector 3-D simulation, including all co-resident antennas. In the past, the incident field characterization has mostly been handled by modeling the transmitting antenna as a line-source at an appropriate location [4]. More complicated models have employed an array of line sources [5]. Experimentally sampling the incident field directly inside the imaging domain has also been reported, wherein the field is then modeled as an exponential damped plane wave [6].

We consider two different calibration methods: incident and scattered. In the incident field calibration, coefficients are calculated based on the incident field measurement versus the modeled incident field [7]. In the scattered field calibration, we place a canonical reference object inside the imaging domain, measure the circuit parameters, then use the assumed incident field

Manuscript received June 15, 2011; revised July 28, 2011; accepted August 23, 2011. Date of publication September 01, 2011; date of current version September 19, 2011. This work was supported by the Natural Sciences and Engineering Research Council of Canada.

M. Ostadrahimi, P. Mojabi, A. Zakaria, and J. LoVetri are with the Department of Electrical and Computer Engineering, University of Manitoba, Winnipeg, MB R3T 5V6, Canada (e-mail: morahimi@ee.umanitoba.ca; pmojabi@ee.umanitoba.ca; azakaria@ee.umanitoba.ca; LoVetri@ee.umanitoba.ca).

C. Gilmore is with CancerCare Manitoba, Winnipeg, MB, R3E 0V9, Canada (e-mail: colin.g.gilmore@gmail.com).

S. Noghanian is with the Department of Electrical Engineering, University of North Dakota, Grand Forks, ND 58202-7165 USA (e-mail: sima@mail.und.edu).

S. Pistorius is with the Department of Physics, University of Manitoba, Winnipeg, MB R3T 5V6 Canada, and also with CancerCare Manitoba, Winnipeg, MB R3E 0V9 Canada (e-mail: Stephen.Pistorius@cancercare.mb.ca).

Color versions of one or more of the figures in this letter are available online at http://ieeexplore.ieee.org.

Digital Object Identifier 10.1109/LAWP.2011.2166849

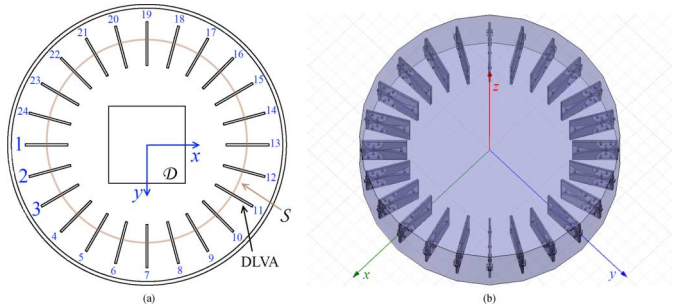

Fig. 1. MWT system of 24 co-resident DLVAs. (a) Imaging domain $\mathcal{D}$ and measurement domain $\mathcal{S}$. (b) Simulation geometry of the full 3-D model.

TABLE I
INCIDENT FIELD MODELING AND CALIBRATION TECHNIQUES

		Calibration technique	
		Incident	Scattered
Incident field	Line-source	$\mathcal{C}_{\mathcal{F}_{\rm ls}}^{\rm inc}$, $E_{\rm ls}^{\rm inc}$	$\mathcal{C}_{\mathcal{F}_{\rm ls}}^{\rm sct}$, $E_{\rm ls}^{\rm inc}$
	3D-model	$\mathcal{C}_{\mathcal{F}_{\rm 3D}}^{\rm inc}$, $E_{\rm 3D}^{\rm inc}$	$\mathcal{C}_{\mathcal{F}_{\rm 3D}}^{\rm sct}$, $E_{\rm 3D}^{\rm inc}$

to calculate the expected scattered field. Coefficients are then created based on these two fields [8]. The canonical reference object is usually an object with high permittivity with respect to the background medium, such as polyvinyl chloride (PVC) in water [6] or a perfect electric conductor (PEC) object [4], [8].

Using these different incident fields and calibration techniques, we analyze the resultant images of experimental datasets collected using our air-based system to determine the effect each parameter has on the imaging results. The mean and standard deviation of the imaging results, as well as the fields, are compared in different regions. Due to the use of different antennas in current MWT systems, with/without a lossy background medium, the associated incident field is different for each system as well as the mutual coupling of the co-resident antennas. A unique calibration method cannot be applied for all tomography systems. However, this letter provides information on the benefits and/or disadvantages of different techniques for a MWT system, when there is no background loss to reduce the mutual coupling.

II. ANTENNAS AND SYSTEM DESCRIPTION

Different antennas have been utilized in co-resident MWT systems. Monopoles [9] and open-ended loaded waveguides [10] seem to be the most popular, probably because they can be replaced by relatively accurate simple models in the inversion algorithm. Nonetheless, we have used more complicated antennas successfully: Our air-based system utilizes 24 co-resident double-layered Vivaldi antennas (DLVA) [11] encircling the OI on the periphery of a plexiglas chamber. The geometry is shown in Fig. 1. The antennas are then connected to a network analyzer through an RF switch network [4].

Due to the heavy computational cost, antennas are not fully modeled in MWT algorithms [3], [10], even for more sophisticated 3-D inversions [9], [12]. Thus, one must determine an acceptably accurate incident field to be used in the imaging algorithm and determine calibration factors that convert the measured quantities to field values at particular positions. The four combinations of the incident field models and the calibration techniques used herein are listed in Table I.

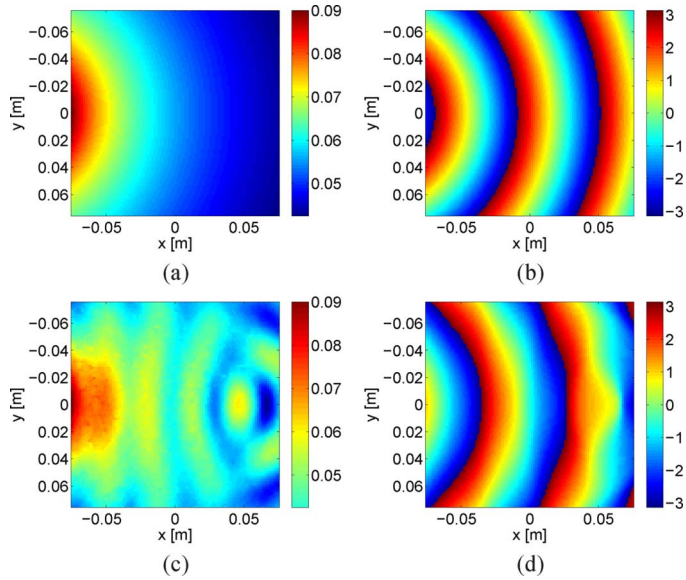

Fig. 2. Antenna #1 incident field amplitude/phase in $\mathcal{D}$ at 5 GHz. (a)$\left|E_{\rm ls}^{\rm inc}\right|$ (V/m). (b) $\angle E_{\rm ls}^{\rm inc}$ (Rad). (c) $\left|E_{\rm 3D}^{\rm inc}\right|$ (V/m). (d) $\angle E_{\rm 3D}^{\rm inc}$ (Rad).

III. FIELD COMPARISON

The imaging and the measurement domains are denoted by $\mathcal{D}$ and $\mathcal{S}$, respectively [see Fig. 1(a)]. The inversion algorithm requires the incident field inside $\mathcal{D}$ as well as the fields at $\mathcal{S}$.

A. Comparing Fields Inside the Imaging Domain

Twenty-four co-resident DLVAs were fully simulated using a 3-D finite element method using the Ansoft HFSS package. The simulation schematic is shown in Fig. 1(b). The incident field is then extracted at the xy-plane ($z = 0$) and is denoted by $E_{\rm 3D}^{\rm inc}$. On the other hand, a line-source model ("ls"), uses line-sources parallel to the z-axis at the DLVA locations. The DLVA source antenna is 7 cm in length, thus the placement of the equivalent line-source is ambiguous and the best location must be found by modeling. Here, we've placed them 1 cm from the front end of the antenna. The incident field of a line-source, denoted by $E_{\rm ls}^{\rm inc}$, is in the form of a Hankel function of the second kind. The amplitude and phase of the $E_{\rm 3D}^{\rm inc}$ and $E_{\rm ls}^{\rm inc}$ inside $\mathcal{D}$ are shown in Fig. 2, where antenna #1 is the transmitter [Fig. 1(a)]. Note that the co-resident array produces fields substantially different from those of a line-source.

B. Comparing Fields on the Measurement Domain

The incident fields from the 3-D model and the line-source model are computed at $\mathcal{S}$, when antenna #1 is the transmitter. The incident field is also measured using the DLVAs' S-parameter measurement [4]. The amplitude and phase for these three cases are shown in Fig. 3(a) and (b). Note that the measurements do not deal with the calibration technique at this time. Next, the field scattered by the PEC calibration object is computed. We first calculated the scattered fields when the transmitter is approximated by a line-source. We then utilized our 2-D forward solver (the method of moments) to compute the scattered fields using the incident field obtained from the 3-D model ($E_{\rm 3D}^{\rm inc}$). Finally we measured the scattered field by the PEC cylinder at 5 GHz, using the DLVAs' S-parameters. The

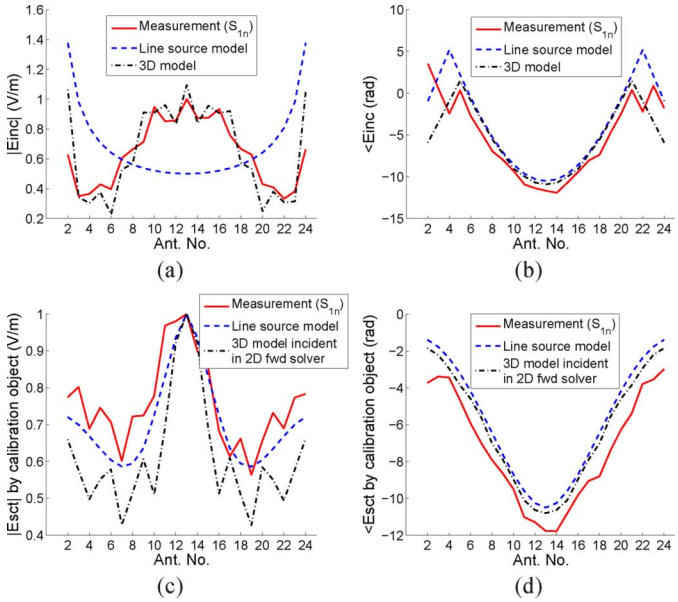

Fig. 3. Comparison of the incident and the scattered fields (by PEC cylinder) on $\mathcal{S}$ at 5 GHz. (a) Incident amplitude. (b) Incident phase. (c) Scattered amplitude. (d) Scattered phase.

amplitude and phase of the scattered field on $\mathcal{S}$ for these three cases are shown in Fig. 3(c) and (d). Again, note the difference between the line-source incident field and the actual field. Also note that the scattered fields are a better match between all three cases than the incident field.

IV. Calibration Coefficients

We denote the incident field calibration coefficients by ${\mathcal{C}_\mathcal{F}}^{\text{inc}}$. For each active transmitter, the ${\mathcal{C}_\mathcal{F}}^{\text{inc}}$ is calculated at the receiver points on $\mathcal{S}$ as

$$ {\mathcal{C}_\mathcal{F}}^{\text{inc}} = \frac{E^{\text{inc}}_{\text{expected}}}{S^{\text{inc}}_{\text{meas}}} \tag{1} $$

where $S^{\text{inc}}_{\text{meas}}$ is the measured S-parameter, corresponding to the incident field, using a network analyzer [4], and $E^{\text{inc}}_{\text{expected}}$ is either from the 3-D model or from the line-source approximation. The corresponding calibration coefficient is denoted by $\mathcal{C}_{\mathcal{F}_{\text{3D}}}^{\text{inc}}$ or $\mathcal{C}_{\mathcal{F}_{\text{ls}}}^{\text{inc}}$, respectively. In the scattered field calibration, for each active transmitter, the calibration coefficient ${\mathcal{C}_\mathcal{F}}^{\text{sct}}$ is calculated at the receiver points on $\mathcal{S}$ as

$$ {\mathcal{C}_\mathcal{F}}^{\text{sct}} = \frac{E^{\text{sct}}_{\text{expected}}}{S^{\text{sct-OIcal}}_{\text{meas}}} \tag{2} $$

where $S^{\text{sct-OIcal}}_{\text{meas}}$ is the measured S-parameter, corresponding to the scattered field by the calibration object, and $E^{\text{sct}}_{\text{expected}}$ is either from the 3-D model or the line-source approximation (as discussed in Section III-B). Note that we use a PEC cylinder, with a 3.5-in diameter, as our calibration object. The corresponding calibration coefficient is denoted by $\mathcal{C}_{\mathcal{F}_{\text{3D}}}^{\text{sct}}$ or $\mathcal{C}_{\mathcal{F}_{\text{ls}}}^{\text{sct}}$, respectively.

Note that we do not use a single calibration coefficient. For each transmitter–receiver pair, the calibration coefficients are calculated individually and are stored in a matrix $\underline{\mathcal{C}_\mathcal{F}}$. The measured scattered fields by an OI, $\underline{S^{\text{sct}}_{\text{meas}}}$, are then calibrated to $\underline{E^{\text{sct}}_{\text{cal}}} = \underline{\mathcal{C}_\mathcal{F}} \odot \underline{S^{\text{sct}}_{\text{meas}}}$, where $\odot$ denotes the Hadamard matrix product of the two matrices $\underline{\mathcal{C}_\mathcal{F}}$ and $\underline{S^{\text{sct}}_{\text{meas}}}$.

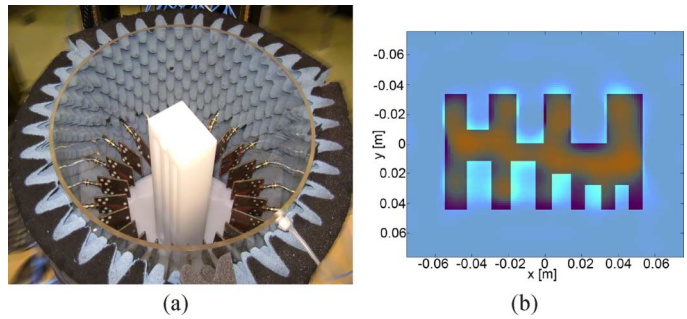

Fig. 4. e-phantom geometry (a) during measurement and (b) overlaid with a reconstructed image.

V. Inversion Results

A complicated dielectric phantom, which we refer to as the "e-phantom," was utilized for image reconstruction. This OI is shown in Fig. 4, and its relative complex permittivity is $\epsilon_{\text{r}} = 2.3 + j0.0$ [13]. The dimensions are reported in [4]. Fig. 4(b) illustrates the OI overlaid with one of the images. The multiplicative regularized GNI algorithm was utilized for image reconstruction [2] with data from the two antennas on either side of the transmitter antenna as well as the backscatterer removed. That is, the dataset consists of $24 \times 21 = 504$ measured points at 5 GHz.

We used both the ${\mathcal{C}_\mathcal{F}}^{\text{inc}}$ (1) and ${\mathcal{C}_\mathcal{F}}^{\text{sct}}$ (2) to calibrate the dataset. The calibration coefficients are computed from both the "ls" and the 3-D models. Thus, four calibrated datasets are generated: $\mathcal{C}_{\mathcal{F}_{\text{ls}}}^{\text{inc}}$, $\mathcal{C}_{\mathcal{F}_{\text{3D}}}^{\text{inc}}$, $\mathcal{C}_{\mathcal{F}_{\text{ls}}}^{\text{sct}}$, and $\mathcal{C}_{\mathcal{F}_{\text{3D}}}^{\text{sct}}$. The corresponding incident field of each calibration coefficient is $E^{\text{inc}}_{\text{ls}}$, $E^{\text{inc}}_{\text{3D}}$, $E^{\text{inc}}_{\text{ls}}$, and $E^{\text{inc}}_{\text{3D}}$, respectively, which are the incident fields used in the domain of the inversion algorithm (see Table I). Imaging results are depicted in Fig. 5 for ${\mathcal{C}_\mathcal{F}}^{\text{inc}}$ and in Fig. 7 for ${\mathcal{C}_\mathcal{F}}^{\text{sct}}$.

For each reconstructed image, the mean and the standard deviation of permittivities were calculated inside the e-phantom boundaries and inside the background medium. The e-phantom and the background boundaries are depicted in Fig. 4(b). These calculations are illustrated in Fig. 6 and provide us a criterion to quantitatively compare the four images. The real and the imaginary parts are calculated separately.

VI. Discussion and Conclusion

The results of Section V and Fig. 6 show that ($\mathcal{C}_{\mathcal{F}_{\text{ls}}}^{\text{inc}}$, $E^{\text{inc}}_{\text{ls}}$) corresponding to Fig. 5(a) and (b) generates artifacts especially in the imaginary part of the image while the real part is not quantitatively accurate. The maximum variance is observed for this case and is due to the error between the line-source model and the real system [see Fig. 3(a) and (b)]. However, by using a more accurate incident field such as the one obtained from the 3-D model, the variance and the mean improves significantly. Compare Fig. 5(c) and (d) to Fig. 5(a) and (b). ($\mathcal{C}_{\mathcal{F}_{\text{3D}}}^{\text{inc}}$, $E^{\text{inc}}_{\text{3D}}$) in Fig. 5(c) and (d) and ($\mathcal{C}_{\mathcal{F}_{\text{3D}}}^{\text{sct}}$, $E^{\text{inc}}_{\text{3D}}$) in Fig. 7(c) and (d) both use $E^{\text{inc}}_{\text{3D}}$ and generate relatively similar and accurate quantitative images, with similar variance and mean. We speculate that the main reason for not seeing considerably improved images when using $E^{\text{inc}}_{\text{3D}}$ is its use in a 2-D imaging algorithm ($\mathcal{C}_{\mathcal{F}_{\text{ls}}}^{\text{sct}}$, $E^{\text{inc}}_{\text{ls}}$), Fig. 7(a) and (b) generates relatively the best qualitative results with the closest mean value to the actual value in the real

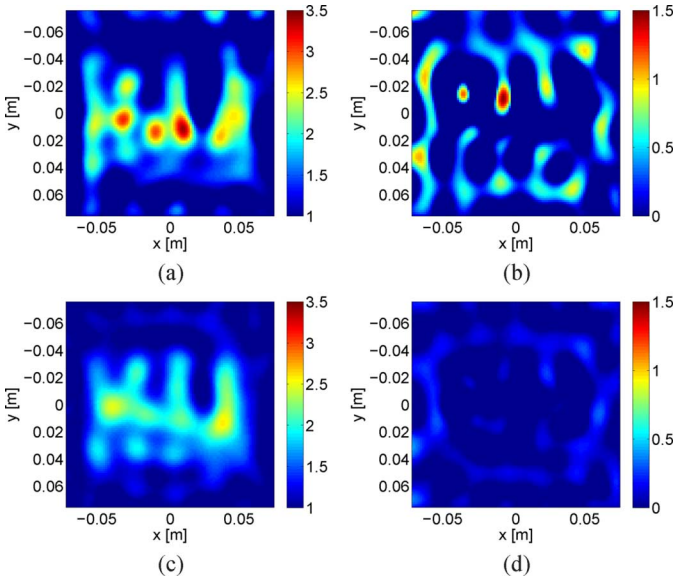

Fig. 5. Complex permittivity reconstruction of the complexity test at 5 GHz using incident field calibration method: $\mathcal{C}_{\mathcal{F}^{\mathrm{inc}}}$. (a) $\mathrm{Re}(\epsilon_r)$: $\mathcal{C}_{\mathcal{F}^{\mathrm{inc}}_{\mathrm{ls}}}, E^{\mathrm{inc}}_{\mathrm{ls}}$. (b) $\mathrm{Im}(\epsilon_r)$: $\mathcal{C}_{\mathcal{F}^{\mathrm{inc}}_{\mathrm{ls}}}, E^{\mathrm{inc}}_{\mathrm{ls}}$. (c) $\mathrm{Re}(\epsilon_r)$: $\mathcal{C}_{\mathcal{F}^{\mathrm{inc}}_{\mathrm{3D}}}, E^{\mathrm{inc}}_{\mathrm{3D}}$. (d) $\mathrm{Im}(\epsilon_r)$: $\mathcal{C}_{\mathcal{F}^{\mathrm{inc}}_{\mathrm{3D}}}, E^{\mathrm{inc}}_{\mathrm{3D}}$.

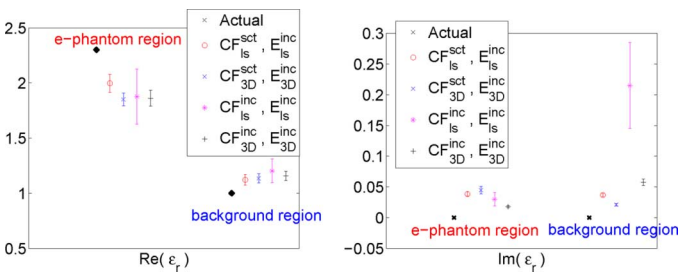

Fig. 6. Mean and standard deviation of reconstructed images.

part of the image. Note that the line-source incident field does not match with the real system, yet there is a good match between the scattered fields from the calibration object [see Fig. 3(c) and (d)].

In conclusion, for our loss-less imaging system, we have found that: 1) scattered field calibration, $\mathcal{C}_{\mathcal{F}^{\mathrm{sct}}}$, generates more accurate quantitative images than does incident field calibration, $\mathcal{C}_{\mathcal{F}^{\mathrm{inc}}}$;, and 2) accurate incident field modeling can improve the images especially when using incident field calibration. We speculate that the scattered field calibration improvement is due to the contribution of the forward solver in $\mathcal{C}_{\mathcal{F}^{\mathrm{sct}}}$ calculation. We also speculate that the 3-D model would improve the imaging result if it was not used within a 2-D algorithm. Although not shown, we have also tested other dielectric phantoms, and similar results were observed.

In addition, this letter provides information for us to verify the incident field modeling in our system. However, the line-source model incorporated with the scattered field calibration is quantitatively and qualitatively similar to a full 3-D model. Thus, we do not need to employ sophisticated procedures to model the incident field such as those outlined herein nor the methods proposed in [5] and [6]. We do note that this letter may generate different results for other antennas and system configurations. However, we expect this result to be common to most other microwave tomography systems.

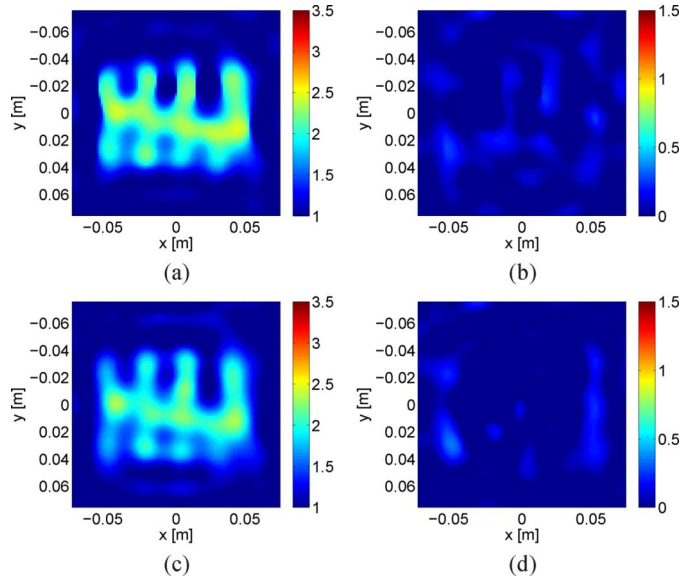

Fig. 7. Complex permittivity reconstruction of the complexity test at 5 GHz using scattered field calibration method: $\mathcal{C}_{\mathcal{F}^{\mathrm{sct}}}$. (a) $\mathrm{Re}(\epsilon_r)$: $\mathcal{C}_{\mathcal{F}^{\mathrm{sct}}_{\mathrm{ls}}}, E^{\mathrm{inc}}_{\mathrm{ls}}$. (b) $\mathrm{Im}(\epsilon_r)$: $\mathcal{C}_{\mathcal{F}^{\mathrm{sct}}_{\mathrm{ls}}}, E^{\mathrm{inc}}_{\mathrm{ls}}$. (c) $\mathrm{Re}(\epsilon_r)$: $\mathcal{C}_{\mathcal{F}^{\mathrm{sct}}_{\mathrm{3D}}}, E^{\mathrm{inc}}_{\mathrm{3D}}$. (d) $\mathrm{Im}(\epsilon_r)$: $\mathcal{C}_{\mathcal{F}^{\mathrm{sct}}_{\mathrm{3D}}}, E^{\mathrm{inc}}_{\mathrm{3D}}$.

REFERENCES

[1] M. Pastorino, *Microwave Imaging*. Hoboken, NJ: Wiley, 2010.
[2] P. Mojabi and J. LoVetri, "Microwave biomedical imaging using the multiplicative regularized Gauss–Newton inversion," *IEEE Antennas Wireless Propag. Lett.*, vol. 8, pp. 645–648, 2009.
[3] C. Gilmore, P. Mojabi, and J. LoVetri, "Comparison of an enhanced distorted born iterative method and the multiplicative-regularized contrast source inversion method," *IEEE Trans. Antennas Propag.*, vol. 57, no. 8, pp. 2341–2351, Aug. 2009.
[4] C. Gilmore, P. Mojabi, A. Zakaria, M. Ostadrahimi, C. Kaye, S. Noghanian, L. Shafai, S. Pistorius, and J. LoVetri, "A wideband microwave tomography system with a novel frequency selection procedure," *IEEE Trans. Biomed. Eng.*, vol. 57, no. 4, pp. 894–904, Apr. 2010.
[5] L. Crocco, M. D'Urso, and T. Isernia, "Testing the contrast source extended Born inversion method against real data: The TM case," *Inverse Problems*, vol. 21, p. S33, 2005.
[6] T. Henriksson, N. Joachimowicz, C. Conessa, and J. Bolomey, "Quantitative microwave imaging for breast cancer detection using a planar 2.45 GHz system," *IEEE Trans. Instrum. Meas.*, vol. 59, no. 10, pp. 2691–2699, Oct. 2010.
[7] P. Meaney, K. Paulsen, and J. Chang, "Near-field microwave imaging of biologically-based materials using a monopole transceiver system," *IEEE Trans. Microw. Theory Tech.*, vol. 46, no. 1, pp. 31–45, Jan. 1998.
[8] J. Geffrin and P. Sabouroux, "Continuing with the fresnel database: Experimental setup and improvements in 3D scattering measurements," *Inverse Problems*, vol. 25, p. 024001, 2009.
[9] T. Rubæk, O. Kim, and P. Meincke, "Computational validation of a 3-D microwave imaging system for breast-cancer screening," *IEEE Trans. Antennas Propag.*, vol. 57, no. 7, pp. 2105–2115, Jul. 2009.
[10] S. Semenov, J. Kellam, Y. Sizov, A. Nazarov, T. Williams, B. Nair, A. Pavlovsky, V. Posukh, and M. Quinn, "Microwave tomography of extremities: 1. Dedicated 2D system and physiological signatures," *Phys. Med. Biol.*, vol. 56, p. 2005, 2011.
[11] M. Ostadrahimi, S. Noghanian, L. Shafai, A. Zakaria, C. Kaye, and J. LoVetri, "Investigating a double layer vivaldi antenna design for fixed array field measurement," *Int. J. Ultra Wideband Commun. Syst.*, vol. 1, no. 4, pp. 282–290, 2010.
[12] Q. Fang, P. Meaney, and K. Paulsen, "Viable three-dimensional medical microwave tomography: Theory and numerical experiments," *IEEE Trans. Antennas Propag.*, vol. 58, no. 2, pp. 449–458, Feb. 2010.
[13] S. Semenov, R. Svenson, A. Bulyshev, A. Souvorov, A. Nazarov, Y. Sizov, V. Posukh, A. Pavlovsky, P. Repin, and G. Tatsis, "Spatial resolution of microwave tomography for detection of myocardial ischemia and infarction-experimental study on two-dimensional models," *IEEE Trans. Microw. Theory Tech.*, vol. 48, no. 4, pp. 538–544, Apr. 2000.